



## Simulation of Arctic snow microwave emission in surface-sensitive atmosphere channels

Melody Sandells<sup>1</sup>, Nick Rutter<sup>1</sup>, Kirsty Wivell<sup>2</sup>, Richard Essery<sup>3</sup>, Stuart Fox<sup>2</sup>, Chawn Harlow<sup>2</sup>, Ghislain Picard<sup>4</sup>, Alexandre Roy<sup>5</sup>, Alain Royer<sup>6</sup>, and Peter Toose<sup>7</sup>

<sup>1</sup>Department of Geography and Environmental Sciences, Northumbria University, Newcastle-Upon-Tyne, UK

<sup>2</sup>Met Office, Exeter, UK

<sup>3</sup>Department of Geosciences, University of Edinburgh, Edinburgh, UK

<sup>4</sup>IGE, Université Grenoble Alpes, Grenoble, France

<sup>5</sup>Département des Sciences de l'Environnement, Université du Québec à Trois-Rivières, Trois-Rivières, Quebec, Canada

<sup>6</sup>Département de géomatique appliquée, Université de Sherbrooke, Sherbrooke, Canada

<sup>7</sup>Climate Research Division, Environment and Climate Change Canada, Toronto, Canada

**Correspondence:** Mel Sandells (melody.sandells@northumbria.ac.uk)

**Abstract.** Accurate simulations of snow emission in surface-sensitive microwave channels are needed to separate snow from atmospheric information essential for numerical weather prediction. Measurements from a field campaign in Trail Valley Creek, Inuvik, Canada during March 2018 were used to evaluate the Snow Microwave Radiative Transfer (SMRT) Model at 89 GHz and, for the first time, frequencies between 118 and 243 GHz. In situ data from 29 snow pits, including snow specific surface area, were used to calculate exponential correlation lengths to represent the snow microstructure and to initialize snowpacks for simulation with SMRT. Measured variability in snowpack properties was used to estimate uncertainty in the simulations. SMRT was coupled with the Atmospheric Radiative Transfer Simulator to account for the directionally-dependent emission and attenuation of radiation by the atmosphere. This is a major developmental step needed for top-of-atmosphere simulations of microwave brightness temperature at atmosphere-sensitive frequencies with SMRT. Nadir simulated brightness temperatures at 89, 118, 157, 183 and 243 GHz were compared with airborne measurements and with ground-based measurements at 89 GHz. Inclusion of an anisotropic atmosphere in SMRT had the greatest impact on brightness temperature simulations at 183 GHz and the least at 89 GHz. Simulations compared well with observations, with a root mean squared error of 14 K, although snowpit measurements did not capture the observed variability fully as simulations and airborne observations formed statistically different distributions. Topographical differences in simulated brightness temperature between sloped, valley and plateau areas diminished with increasing frequency as the penetration depth within the snow decreased and less emission from the underlying ground contributed to the airborne observations. Observed brightness temperature differences between flights were attributed to the deposition of a thin layer of very low density snow. This illustrates the need to account for both temporal and spatial variability in surface snow microstructure at these frequencies. Sensitivity to snow properties and the ability to reflect changes in observed brightness temperature across the frequency range for different landscapes, as demonstrated by SMRT, is a necessary condition for inclusion of atmospheric measurements at surface-sensitive frequencies in numerical weather prediction.



## 1 Introduction

Numerical weather prediction (NWP) is challenging in the Arctic due to lack of observations suitable for assimilation (Geer et al., 2014). Consequently Arctic NWP is not as accurate as for midlatitudes (Randriamampianina et al., 2021). Sparse population and extreme conditions mean that ground-based observations that could be used for assimilation are few and far-between and/or have bias in their spatial distribution (Bauer et al., 2016). In contrast, there is a wealth of satellite data at high temporal resolution at high latitudes (Lawrence et al., 2019). Atmosphere sounding data are routinely assimilated into NWP in order to initialise the forecasts. However, data over Arctic regions are frequently discarded because of the difficulty in accounting for the surface component (Guedj et al., 2010; Karbou et al., 2014; Bauer et al., 2016; Hirahara et al., 2020).

Previous research has indicated potential benefits of the assimilation of microwave data over Arctic regions, and that forecast improvements may extend to lower latitudes in the medium-range (Guedj et al., 2010; Karbou et al., 2014; Day et al., 2019), with some uncertainty in mechanisms and magnitude (Cohen et al., 2014; Overland et al., 2015). Extreme weather events in the mid-latitudes have been linked to air-mass transformation processes and Arctic amplification (Francis and Vavrus, 2012; Pithan et al., 2018; Overland et al., 2021). Mid-latitude observations have also been shown to have a strong impact on Arctic medium-range forecasts during summer (Lawrence et al., 2019). Data denial experiments within the European Centre for Medium Range Weather Forecasts NWP system highlighted the dominant impact of microwave sounding data in summer compared with winter. This was attributed in part to the reduction in number of observations used in the winter, and points to the potential benefits of improved methods of using these data (Lawrence et al., 2019).

Microwave observations from 19-243 GHz are sensitive to both atmosphere and surface conditions to varying degrees. Atmospheric window frequencies around 19, 37 and 89 GHz are used to obtain information about the surface (e.g. snow) as they are less sensitive to the atmosphere. Atmospheric sounding channels are more sensitive to the atmosphere than the surface. Frequencies around 60 and 118 GHz (oxygen absorption bands) are used to infer atmospheric temperature profile information, whereas humidity profile information is obtained from water vapour channels around 183 GHz. In the dry Arctic winter, 157 GHz can be considered a window channel. Baordo and Geer (2016) demonstrated improvements in the forecast analysis through assimilation of humidity sounding channels (183 GHz) over land in all-sky (cloudy and clear) conditions with retrieved emissivity, but an emissivity database was used for latitudes greater than 60° and surface temperatures less than 278 K because of difficulty in specifying surface emissivity in snow-covered environments. Particularly over snow, the microwave emissivity is highly spatially variable and has high uncertainty as it is sensitive to the microstructure (grain size, shape and spatial arrangement at the micrometer scale) of the snow. To account for the influence of the snow on satellite atmospheric observations, the microstructure of the snow must be known well, and an accurate model of microwave scattering in snow is required to interpret the observations (Harlow and Essery, 2012; Bormann et al., 2017; Wang et al., 2017; Lawrence et al., 2019; Hirahara et al., 2020).

Numerous snow microwave scattering models have been developed with a focus on remote sensing of snow properties (e.g. Wiesmann and Mätzler, 1999; Tsang et al., 2000; Lemmetyinen et al., 2010; Ding et al., 2010; Picard et al., 2013) with no single model outperforming another (Sandells et al., 2017; Royer et al., 2017). Previous research has led to greater



understanding into different microwave behaviour between these models due to relative impacts of the microstructure model, electromagnetic model and radiative transfer solver approach (Löwe and Picard, 2015; Pan et al., 2015; Picard et al., 2018). Further understanding of model differences is facilitated through the modular structure of the Snow Microwave Radiative Transfer (SMRT) model, developed to isolate and quantify uncertainty in snow microwave scattering processes as a result of the theoretical model configuration (Picard et al., 2018). Sandells et al. (2021) evaluated SMRT against ground-based data over natural snowpacks in the 5-89 GHz range and obtained root mean squared errors of 3-12 K with Gaussian Random Field or Teubner-Strey microstructure parameters derived from X-ray tomography and thin section images, demonstrating accuracy comparable to, or better than, other microwave scattering model evaluation studies that required optimization of the snow microstructure to obtain good agreement with observations. Through comparisons with airborne data over tundra snow at 89, 157 and 183 GHz, Harlow and Essery (2012) demonstrated a need for either surface roughness to be taken into account or a limitation placed on the microstructure-dependent scattering coefficient at these higher frequencies in order to explain the observed emissivity spectra with the emission model used. As snow microstructure information was not available in the Harlow and Essery (2012) study, a detailed evaluation of the microwave emission model was not possible. To our knowledge, no previous studies have attempted evaluation of snow scattering models at higher frequencies useful for NWP given measured snow microstructure information.

In this study we evaluate SMRT simulated brightness temperatures (TB) against airborne data at five frequencies (89, 118, 157, 183 and 243 GHz) given in situ measured microstructure information. The purpose of this study is to demonstrate that SMRT can sufficiently explain the behaviour of observed airborne TB at these frequencies, required to improve assimilation of satellite data in numerical weather prediction. A novel component of this is the coupling of SMRT with the Atmosphere Radiative Transfer Simulator (ARTS) (Buehler et al., 2018) to account for emission and attenuation by the anisotropic atmosphere at these higher frequencies. Data used in this study were taken as part of the MACSSIMIZE (Measurements of Arctic Clouds, Snow and Sea Ice nearby the Marginal Ice Zone) field campaign in Trail Valley Creek (TVC), NWT, Canada in March 2018. During the campaign, multiple ground based profiles of snow specific surface area were obtained and other stratigraphic physical properties measured at multiple snow pit locations across the study area. These ground-based observations were described and analyzed in Rutter et al. (2019). Here, we use data from the 2018 field campaign to drive passive SMRT simulations at each of the snowpit locations and compare TB with limited ground-based radiometer observations at 89 GHz and with airborne TB at 89 GHz and higher frequencies. The paper is structured as follows: section 2 describes the TVC site and ground data, collection and processing of airborne data, methodology of the SMRT simulations and correction of TB to the level of the aircraft. SMRT simulations are compared with the ground-based radiometer observations and airborne observations in section 3, with discussion and conclusions presented in sections 4 and 5. Access information to obtain data and code is given in section 5.

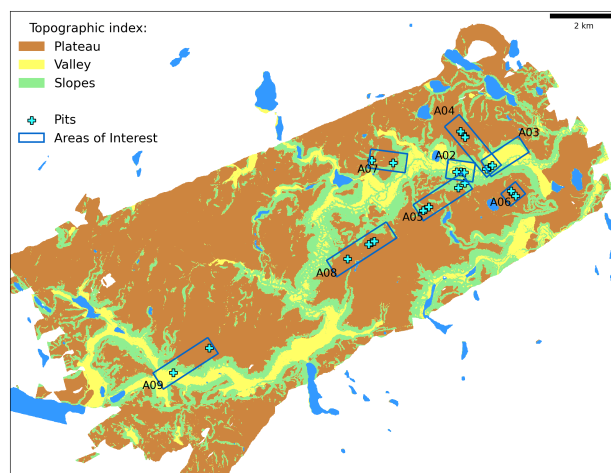


**Figure 1.** Topographic index of Trail Valley Creek, NWT, Canada with locations of snow pits and Areas Of Interest for airborne data. Adapted from Rutter et al. (2019).

## 2 Methods

### 2.1 Ground Data

Ground-based measurements of snow microstructure and microwave emission were made throughout the catchment of Trail Valley Creek (TVC), NWT, Canada ( $68^{\circ}44'17''$  N  $133^{\circ}26'26''$  W) between 14-22 March 2018. Figure 1 shows how the catchment was topographically divided into areas of flat upland plateau ( $< 5^{\circ}$  ground slope), flat valley bottom ( $< 5^{\circ}$ ) and slopes ( $> 5^{\circ}$ ) (Rutter et al., 2019) and highlights Areas of Interest (AOIs) selected for study prior to the field measurements. Further contextual information about seasonal changes in TVC and drone-based structure-from-motion snow depth measurements within the AOIs are available in Walker et al. (2021), with some differences in AOI numbering and dimensions from this study. Snow-pit measurement locations (Figure 1) were selected in order to capture a wide range of topographies, aspects and vegetation characteristics of TVC, which are also representative of the wider Arctic tundra in general. In addition, snowpit locations were linearly aligned along three flight lines to allow spatially coincident comparisons of airborne measurements with measured and simulated microwave emissions from the surface.

Vertical profiles of snow properties (density, Specific Surface Area (SSA), temperature, stratigraphy) required to simulate microwave scattering in snow were measured in 29 snowpits. In each pit, density, SSA and temperature were measured at a 3 cm vertical resolution. Densities were measured using a  $100\text{ cm}^3$  gravimetric cutter and SSA was measured using two measurement systems, an InfraRed Integrating Sphere (IRIS) (Montpetit et al., 2012) and an A2 Photonic Sensors IceCube, both of which followed the method of Gallet et al. (2009) using infrared reflectance of snow samples at 1310 nm in an integrating sphere. For density and SSA, the average of two replicate samples at each position in the vertical profile were taken in the majority of snowpits in order to account for horizontal heterogeneity across the snowpit wall. Snowpack layers (including ice lenses) were

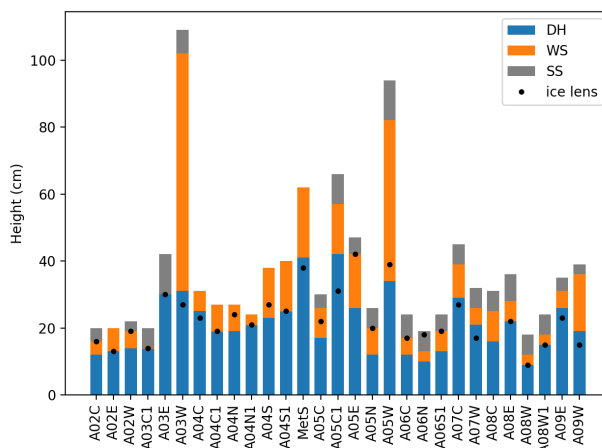


**Figure 2.** Stratigraphy of individual snowpits within Areas of Interest. Depth hoar layers (DH) are shown in blue, wind slab layers (WS) are shown in orange and surface snow (SS) is shown in grey. The location of ice lenses is shown by the black dots.

identified through visual inspection and hardness tests, and classified according to Fierz et al. (2009). Additionally, following Rutter et al. (2019), snow layers were grouped into one of three microstructure types: surface snow (SS), wind slab (WS), or depth hoar (DH), through comparative assessment of all profile measurements in combination with each other, shown in Figure 2. The majority of snowpits were between 20 and 40 cm deep. Pits A03W and A05W were located in drifts, leading to depths closer to 1 m. Depth hoar was present in all pits. Pit A03E did not have a wind slab layer, and only a thin wind slab layer was present in A03C1. Several pits did not have a fresh surface snow layer present. Almost all pits had an ice crust present, with the exception of pit A08C.

At ten pit locations, coincident measurements of passive microwave brightness temperature (TBs) at 89 GHz, in both vertical and horizontal polarizations, were made by a surface-based radiometer (Langlois, 2015). The radiometer was mounted on a sled at a height of approximately 1.5 m above, and at an angle nadir to, the snow surface. A 6 dB beam width of 3° meant the measurement footprint on the snow surface was approximately 0.15 m x 0.15 m. Radiometers were calibrated using ambient (black body) and cold (liquid nitrogen) targets and had a worst case measurement error of 2 K based on 6 ambient black body calibration checks made during the campaign. At each location, TBs measurements were made over a 6-second integration time for a minimum of three minutes. Mean TBs were calculated and the standard deviation used as a quality control flag. Three measurements were made at each site and the radiometer was moved by 2.5 m between each measurement. Coincident physical temperatures were made at both the base and within the snowpack.

## 2.2 Airborne Data

During MACSSIMIZE the Facility for Airborne Atmospheric Measurements (FAAM) BAe-146 atmospheric research aircraft was based in Fairbanks, Alaska. Five flights were flown over TVC and followed a series of low-level flight lines which aligned



Centre frequency (GHz)	Frequency offset (GHz)	Intermediate Frequency Bandwidth (GHz)	Feature	Approximate Footprint from aircraft height (~ 500 m)
88.992	±1.075	0.65	Window	100 m
118.75	±5.0	2.0	O <sub>2</sub>	30 m
157.075	±2.6	2.6	Window	100 m
183.248	±7.0	2.0	H <sub>2</sub> O	50 m
243.2	±2.5	3.0	Window	30 m

**Table 1.** MARSS and ISMAR channel definitions for frequencies used in this study

125 with the snowpits. This paper focuses on data for two flights, C087 and C090, on the 16<sup>th</sup> and 20<sup>th</sup> March 2018, as these flights were free of low cloud and occurred within the same period as ground observations were made. Airborne measurements were taken using the Microwave Airborne Radiometer Scanning System (MARSS; McGrath and Hewison, 2001) and the International Submillimetre Airborne Radiometer (ISMAR; Fox et al., 2017) on board the FAAM aircraft. Both instruments are along-track scanning radiometers containing dual-sideband heterodyne receivers measuring between 89 and 664 GHz. This paper concentrates on channels up to 243 GHz as frequencies higher than this will not have significant sensitivity to the surface except in very dry environments due to strong water vapour absorption. A summary of the channels used in this study is given in Table 1. Processing of MARSS and ISMAR data produces Rayleigh-Jeans equivalent TBs (Fox et al., 2017).

135 The radiometers are mounted on the side of the aircraft, allowing both upward and downward views, and contain a rotating scan mirror with a fully configurable scan pattern. A typical scan cycle rotates through multiple upward and downward scene views, plus views of two calibration targets (one ambient and one heated). During MACSSIMIZE the instruments remained at a single downward viewing angle when over the AOIs, with calibration and zenith views in between, to increase the number of observations taken over the surface sites. This paper uses observations where the instruments pointed in a near-vertical nadir direction ( $\pm 5^\circ$ ) when over the AOIs, which occurred during C087 and two runs of C090. Most of the MARSS and ISMAR receivers detect a single linear polarisation (of the channels studied in this paper only the 243 GHz window channel offers dual orthogonal polarisation) with the polarisation angle depending on the instrument scan angle. This must be considered for non-nadir observations; however in this paper only near-vertical nadir observations are used where the impact of polarisation angle is minimal.

### 2.3 SMRT Modelling

145 The Snow Microwave Radiative Transfer (SMRT) model was previously described in Picard et al. (2018). Briefly, this is a multilayer snow scattering model suitable for passive, active and radar altimeter applications (Larue et al., 2021). It has a modular structure that allows different modelling configurations, including electromagnetic model and radiative transfer solver. For the simulations presented in this paper the Improved Born Approximation electromagnetic model and DORT radiative transfer



150 solver were used to simulate brightness temperature emitted from the surface of the snowpack, given snowpack properties described later in this section. SMRT was coupled with ARTS to account for atmospheric emission and absorption necessary at these higher frequencies and to simulate TB at the height of the aircraft. Results presented in this paper use nadir, vertically polarized TB to evaluate SMRT against ground-based and airborne observations. Atmospheric correction of the ground-based radiometric data to the height of the aircraft for comparison with airborne data is described later in section 2.4.

155 ‘Base’ SMRT simulations describe default parameterisations and neglect within-layer measurement variability or other potential sources of error considered later in this study. These base simulations were constructed from the three-layer dataset described in section 2.1 and shown in Figure 2. Observations of layer thickness, temperature and density were used directly to create SMRT layers. However, SMRT requires microstructure model parameters rather than the SSA observed in the field. To link with previous studies (Harlow and Essery, 2012; King et al., 2018; Vargel et al., 2020), an exponential microstructure model was chosen for this study. SSA was used to derive the required exponential correlation length with the modified Debye relationship (Mätzler, 2002; Montpetit et al., 2012):

$$160 \quad l_{ex} = \alpha_{db} \frac{4(1 - \rho/\rho_i)}{SSA\rho_i} \quad (1)$$

where the Debye modification parameter  $\alpha_{db}$  is assumed to be 0.75 for surface snow and wind slab layers (Mätzler, 2002) and 1.2 for depth hoar (Leinss et al., 2020) in the base simulations,  $\rho$  is the snow density and  $\rho_i$  is the density of pure ice. The value of  $\alpha_{db}=1.2$  for depth hoar was chosen after initial assessment of the modelling strategy through a sensitivity study described below. For snowpits with dual density and SSA observation profiles, the mean layer values between profiles were used in the base simulations. Table 2 illustrates the density and SSA values used for each pit and the values taken from Rutter et al. (2019) used for missing observation values in layers that were too thin. The underlying soil surface is assumed to be flat, with a temperature of 258.15 K and permittivity of 4–0.5j based on the work of King et al. (2018) at TVC. As snowpit observations were made over an eight-day period under varying atmospheric conditions, SMRT snow layer temperatures were linearly interpolated from the air temperature at the time of the flights to the mean of the measured temperatures (263 K) in the lowest snow layer on flight days.

170 An ice lens was present in almost all snowpits, but occurred at different locations within the layers as shown in Figure 2. Where ice lenses were present, an additional layer was inserted into the snowpack. The recorded height of the ice lens was used to inform the strategy for amending the layering structure of the snow. As illustrated in Figure 3, for an ice lens at the boundary between layers, the thickness of the lower layer is reduced in order to maintain the correct total snow depth and the ice lens inserted, leading to a four-layer snowpack. If the ice lens occurs within a layer, then that layer is split with the thickness of the top section given by the height of the top of the layer minus the height of the top of the ice lens. The thickness of the lower section is recalculated to maintain total snow depth. This results in a five-layer snowpack to represent an ice lens embedded within one of the three original layers. The ice lens density is assumed to be  $909 \text{ kg m}^{-3}$  (Watts et al., 2016) and SSA assumed to be  $100 \text{ m}^2 \text{ kg}^{-1}$  (extremely weakly scattering, mainly boundary effects), with ice lens thickness given by the field measurements.



**Table 2.** Snow pit properties used for base SMRT simulations. Density and Specific Surface Area (SSA) are given for the Surface Snow (SS), Wind Slab (WS) and Depth Hoar (DH) layers. In layers that were too thin to measure, properties were gap-filled from the ‘Missing data’ values taken from Rutter et al. (2019). Flight overpass data used in this paper were from 16<sup>th</sup> March and 20<sup>th</sup> March 2018.

Pit	Date	Depth [m]	Density [kg m <sup>-3</sup> ]			SSA [m <sup>2</sup> kg <sup>-1</sup> ]			Topographic Index
			SS	WS	DH	SS	WS	DH	
A02C	15/03/2018	0.2	-	298	255	-	22.0	8.7	Valley
A02E	15/03/2018	0.2	-	328	282	-	30.8	13.5	Valley
A02W	14/03/2018	0.22	252	323	249	31.6	19.6	12.8	Valley
A03C1	17/03/2018	0.2	40	-	230	31.1	-	13.8	Valley
A03E	17/03/2018	0.42	159	-	264	44.7	-	10.0	Valley
A03W	17/03/2018	1.09	132	368	270	43.5	31.0	13.2	Slope
A04C	16/03/2018	0.31	-	314	226	-	22.8	12.0	Plateau
A04C1	16/03/2018	0.27	-	271	297	-	27.1	10.1	Plateau
A04N	16/03/2018	0.27	-	302	272	-	15.9	10.4	Plateau
A04N1	16/03/2018	0.24	-	232	265	-	33.2	18.3	Plateau
A04S	16/03/2018	0.38	-	332	257	-	26.0	13.4	Plateau
A04S1	16/03/2018	0.4	-	308	262	-	23.8	13.1	Plateau
MetS	22/03/2018	0.62	-	297	252	-	34.3	16.0	Plateau
A05C	21/03/2018	0.3	96	380	246	48.5	23.3	11.2	Slope
A05C1	20/03/2018	0.66	60	324	251	32.3	24.5	10.6	Plateau
A05E	20/03/2018	0.47	65	310	257	41.5	17.4	12.3	Plateau
A05N	21/03/2018	0.26	58	367	277	47.6	20.5	13.0	Slope
A05W	20/03/2018	0.94	75	336	202	46.1	28.1	12.0	Plateau
A06C	18/03/2018	0.24	158	310	244	40.0	-	10.6	Plateau
A06N	18/03/2018	0.19	52	222	216	48.4	51.6	13.2	Plateau
A06S1	18/03/2018	0.24	60	285	222	38.2	12.9	9.4	Plateau
A07C	21/03/2018	0.45	86	299	263	48.7	26.6	11.3	Slope
A07W	21/03/2018	0.32	76	336	269	51.9	34.6	15.3	Plateau
A08C	20/03/2018	0.31	90	287	238	48.6	18.8	12.0	Plateau
A08E	20/03/2018	0.36	73	421	283	52.8	28.1	11.7	Plateau
A08W	20/03/2018	0.18	94	250	196	51.0	21.9	8.6	Plateau
A08W1	20/03/2018	0.24	80	205	258	56.4	17.8	9.9	Plateau
A09E	20/03/2018	0.35	127	319	292	58.4	22.1	14.6	Plateau
A09W	20/03/2018	0.39	38	307	349	88.2	35.6	14.2	Valley
Missing data	-	-	104	316	253	44.7	23.8	11.5	-



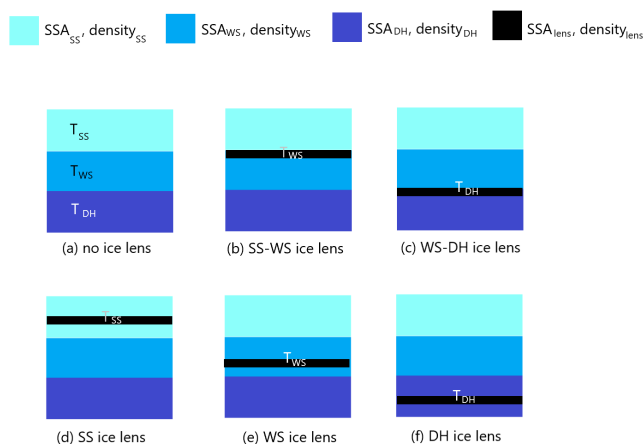


**Figure 3.** Modelling strategy to account for ice lenses in 3-layer snowpack

Uncertainty associated with the simulation approach was assessed using pit A04N as a case-study at 89 GHz. At this frequency, simulations are expected to be more sensitive to processes lower in the snowpack than at other frequencies. Phenomena observed in some pits but not accounted for in the base simulations include air gaps at the snow-soil interface and formation of surface crusts. There is also variability in observed depth, SSA and density. Finally the modified Debye parameter  $\alpha_{db}$  is not known but often taken as 0.75 from Mätzler (2002). Leinss et al. (2020) indicated this value may be as high as 1.2 for depth hoar, which is within the range found by Vargel et al. (2020), who considered variability in this parameter with frequency and snow type. Here for simplicity we compare the case where all layers have  $\alpha_{db}=0.75$  with the case where the depth hoar layer has  $\alpha_{db}=1.2$ .

Sensitivity of simulated TB to modelling assumptions is shown in Table 3. A basal air gap was included by inserting a 5 mm layer of low density ( $10 \text{ kg m}^{-3}$ ) snow and exponential correlation length of  $10 \mu\text{m}$ . This, however, had a negligible effect on the TB, as did incorporating a depth observation uncertainty of 2 cm (applied to the depth hoar layer thickness). Including a surface crust of thickness 5 mm with ice lens density and exponential correlation length of 10 microns lowered the TB by 4.5 K. A more realistic Debye modification of 1.2 applied to only the depth hoar layer resulted in a larger drop in TB of 5.7 K. This impact cannot be ignored and demonstrates a potential deficiency in the use of the ‘standard’ Debye correction factor of 0.75. However, the largest impact on TB was found by representing the layer density and SSA by the largest and smallest observed values. Including all effects resulted in a TB range of 164-193 K, close to the full range of plateau airborne observations for A04, which was 163-201 K.

All simulations presented in the results section use the new Debye modification of 1.2 for the depth hoar layer (0.75 for all other layers). Surface crusts are neglected due to the difficulty in determining whether they are present or not, but could



**Table 3.** Sensitivity results for snow pit A04N, used to define modelling protocol based on a comparison with airborne observations at 89 GHz over plateau regions of A04. Effect of flight C087 atmosphere (see section 2.4) included.

Scenario	Median TB [K]	Low TB [K]	High TB [K]
a: modified Debye = 0.75	185.63		
b: modified depth hoar Debye = 1.2	179.95		
c: basal air gap	185.49		
d: surface crust	181.16		
e: SSA and density extremes		167.44	207.50
f: depth uncertainty		185.79	185.52
b + c + d + e + f		163.96	192.69
b + e		164.60	198.97
<b>A04 Plateau Observations</b>	<b>180.60</b>	<b>162.91</b> (min) <b>171.74</b> (25%ile)	<b>201.01</b> (max) <b>191.74</b> (75%ile)

200 be a source of error. Basal air gaps and uncertainty in depth are neglected due to the lack of sensitivity to them. ‘Base case’ simulations are driven by the median in microstructural properties, but the minimum and maximum measurements of SSA and density are also used to determine variability in simulations. Including atmospheric effects, this leads to a simulated TB range of 165-199 K for pit A04N (scenario b + e in Table 3), comparable to the airborne observations.

## 2.4 Atmospheric Correction

205 For this paper the Atmospheric Radiative Transfer Simulator (ARTS; Eriksson et al., 2011; Buehler et al., 2018) has been used to simulate the angular-dependent atmospheric radiation for SMRT. The simulated atmosphere accounts for the atmospheric downwelling contribution to the surface signal (radiation transmitted into the snowpack and radiation reflected by the surface) that distinguishes simulations for each flight day, and is used to correct for the layer of atmosphere between the aircraft and the surface when comparing airborne observations to surface-based radiometer observations and simulations. Surface TB were  
210 corrected to aircraft height using

$$T_{b,corr}(\theta,\nu) = Tr(\theta,\nu)T_{b,s}(\theta,\nu) + T_{b,up}(\theta,\nu), \quad (2)$$

where  $T_{b,corr}$  is the corrected surface TB at angle  $\theta$  and frequency  $\nu$ ,  $Tr$  is the atmospheric transmission which determines the attenuation of the surface signal,  $T_{b,s}$  is the uncorrected surface TB (which includes downwelling atmospheric radiation scattered by the snow) and  $T_{b,up}$  is the upwelling TB due to atmospheric emission.

215 The atmospheric impact is expected to be greatest for the atmospheric sounding channels due to absorption and emission by oxygen (118 GHz) and water vapour (183 GHz). However the atmospheric window channels (89, 157 and 243 GHz) also have some sensitivity to the atmosphere due to the water vapour continuum and far wings of water vapour and oxygen absorption



lines. In this paper the channels furthest from the centre of the atmospheric absorption lines at 118 and 183 GHz were chosen because strong oxygen and water vapour absorption at the channels closer to the absorption line centres mean there is little sensitivity to the surface, and these channels would be less useful for verifying SMRT.

Temperature and water vapour profiles used as input for ARTS were retrieved for each AOI in each flight. Background profiles were taken from a combination of profiles from the Met Office operational global NWP model (above aircraft height) and dropsonde profiles (below aircraft height) from dropsondes released before the low-level AOI runs. The retrieval adjusts these background profiles in order to match the aircraft-level downwelling observations in the vicinity of each AOI at  $183 \pm 1$ ,  $\pm 3$  and  $\pm 7$  GHz. The height at the bottom of each profile is determined by interpolating to the mean ground height of the AOIs. Due to the instruments remaining at nadir over the AOIs, downwelling observation data at the full range of zenith viewing angles has been taken for a period 30 seconds either side of the AOI overpass.

Within ARTS, water vapour absorption is calculated using the AER v3.6 line parameters with the MTCKD v3.2 continuum. Oxygen absorption is calculated using the Tretyakov et al. (2005) model. Simulated downwelling TBs using the ARTS absorption model configuration mentioned here are compared with observations in the Supplementary material A1 for the full range of zenith viewing angles. The figure in Appendix A1 demonstrates how atmospheric downwelling varies with viewing angle and therefore why it is important to represent the atmosphere as anisotropic.

SMRT and therefore the ARTS configuration used return thermodynamic TBs. As stated in section 2.4, MARSS and IS-MAR processing produces Rayleigh-Jeans equivalent TBs and therefore SMRT simulations are converted to Rayleigh-Jeans equivalent before comparison with airborne observations by applying a frequency dependent offset given by  $h\nu/2k$ , where  $h$  is Planck's constant,  $\nu$  is frequency and  $k$  is Boltzmann's constant. A discussion of the different TB definitions and the derivation of the offset can be found in Han and Westwater (2000).

### 3 Results

#### 3.1 SMRT Evaluation Against Ground Data

Figure 4 compares SMRT TB at 89 GHz with nadir ground-based TBs measured by the sled-mounted radiometers. SMRT simulations are the mean of the two flights, then corrected to ground-level with the inversion of equation 2. The range of simulations capture the observations with the exception of pits A06S1 (plateau pit) and A03C1 (valley pit). The low TB simulated in A03C1 is later attributed to a very low surface density whereas low wind slab SSA drives the discrepancy in A06S1 (see section 3.2). The base simulations (shown by blue circles) tend to overestimate high TB and underestimate low TB. Overall the mean error is -7.1 K and root mean squared error is 16.6 K. Removal of outliers A03C1, A06N and A06S1 reduces the mean error to -0.03K and root mean squared error to 7.5K.

Ground-based radiometer observations were corrected to the height of the aircraft and compared with airborne observations in Figure 5. Airborne observations include all those within the AOI and over the same topography classification as the pit, with the central point showing the median value and error bars indicating the interquartile range. Most observations are grouped, but with larger variability in the ground-based observations. Pits A03W (slope) and A05W (plateau) had a much higher TB

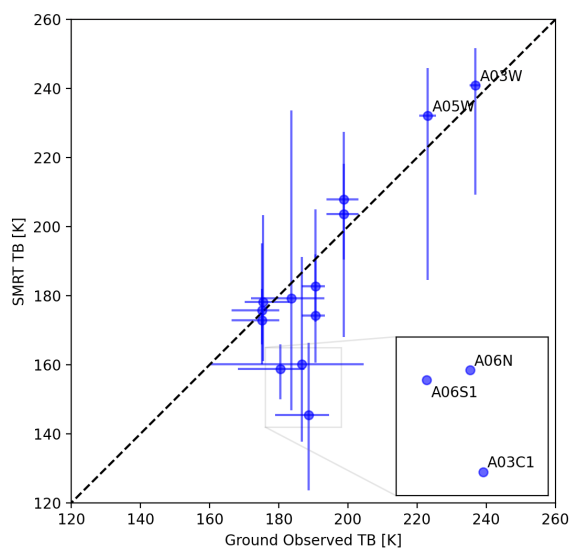


**Figure 4.** Comparison between SMRT simulations and ground-based radiometer observations at 89 GHz, nadir

observed on the ground than from the aircraft. These pits had the deepest snow, as shown in Figure 2, and were located in drifts. Figure 5 illustrates the challenges in using airborne data to evaluate ground-based point simulations, given that the footprint may be different in size and location.

Differences in ground vs airborne footprint location are shown in Figure 6, where data from the C087 flight have been plotted according to their calculated ground co-ordinates. Some areas of interest have pits (shown by crosses) relatively close to the line of flight e.g. A07, A09 whereas others e.g. A05, A06, A08 have a line of pits parallel to the flight data. TB along the airborne transects appear to show a topographic signal: plateau areas tend to have low TB and sloped or transition areas high TB. This is shown clearly in A07 in Figure 6, but is evident in other areas of interest. Some transects contain TB signatures not easily identifiable from the topographic map (e.g. high TB in North East of A08), but could be due to smaller scale heterogeneity in the underlying surface, the snow properties or vegetation. Given the difference in footprint location, it is plausible that selection of the closest airborne TB may not be representative of TB at pit locations as the underlying topography may be very different. Because of the difficulties of matching a given snowpit location with a representative airborne footprint, for comparison with SMRT simulations, all airborne observations over a particular topography class (plateau, slope, valley) were grouped within each AOI. In this way, valley pit simulations were compared with all the valley airborne observations within its AOI, and likewise for the pits located on slopes and on the plateau.

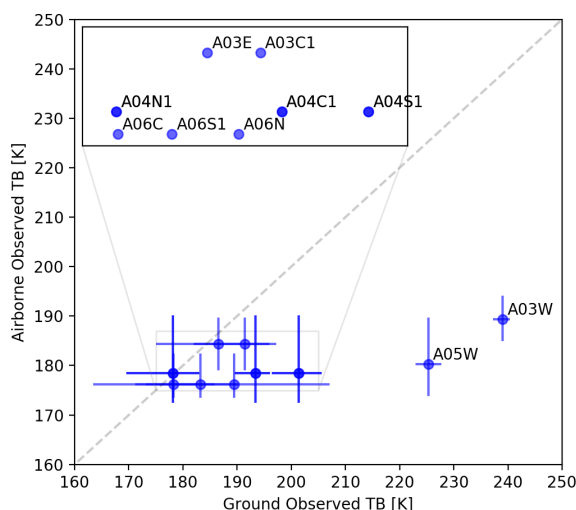


**Figure 5.** Comparison between ground based observations of brightness temperature and airborne brightness temperature at 89 GHz for pits where observations were available. Airborne observations from both C087 and C090 flights were used, and ground-based observations have been corrected to height of aircraft.

### 3.2 SMRT Evaluation Against Airborne Data

Figure 7 compares the simulated TB from each of the 29 pits with the airborne observations within the same AOI and topographical index. Simulated TB at 29 pits overlapped airborne TB range in all but four pits, examined in further detail later in this section. SMRT had good agreement with ground-based TB at A03W but not at A03C1 or A06S1, consistent with Figure 4. Ground-based TB was not available for the Met Station snowpit. Analysis of pits grouped by their underlying topography (see Table 2) provides a test of how well SMRT simulations are able to explain the observed broad-scale spatial variability in TB.

Valley pits in A02 are simulated well, with overlap between simulations and observations. The western (A02W) base simulation (blue hexagon) lies within the airborne whiskers. Variability in microstructure parameters in the Eastern and Central pits A02E and A02C leads to a larger range in simulated TB that overlaps the median of airborne TB, demonstrating that SMRT can be used to represent airborne TB adequately. Other valley pits (A03E, A09W and A03C1) also have a large range in simulated TB. There is close agreement between airborne median TB, ground TB and SMRT base simulation despite the large variation in microstructure at valley pit A03E. SMRT underestimates TB at valley pit A03C1. Table 2 indicates pit A03C1 also had an unusually low surface density. If the *missing data* value from Table 2 is used in the base simulation instead of the low surface density, TB increases from 149.3 K to 156.2 K and is therefore much closer to the observations.

Four snowpits were dug in areas classified as sloped topography. These were A03W, A05C, A05N and A07C. At A03W, SMRT simulations are higher than and outside of the range of airborne observations. There is, however, close agreement with ground TB measurements indicating that the airborne observations may not have observed the drift containing A03W. The

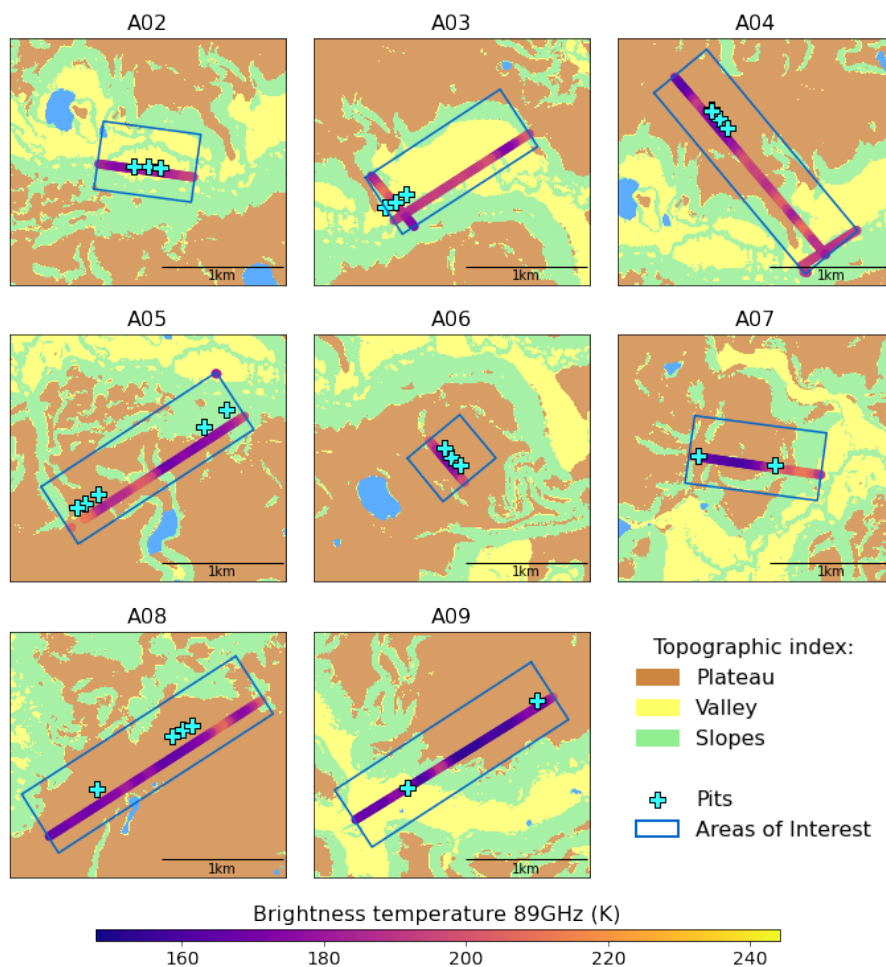


**Figure 6.** Variation in flight C087 observed airborne brightness temperature in each Area of Interest. Snow pit locations are indicated with crosses.

remaining slope pits show good agreement with airborne observations, with A05C SMRT simulations covering the interquartile range of the airborne observations and A05N and A07C simulations covering the extent of the whiskers. For pit A07C, the simulations also capture the few low TB outliers.

Plateau pits are generally simulated well with the exception of the Met Station and A06S1. Simulated TB at the Met Station is too high compared with airborne observations, which indicates an underestimation of scattering. The Met Station is situated in A04 along with three sets of paired pits. Observations A04C and A04C1 were made in adjacent pits, and the ground-based radiometric observations taken at location A04C1 were assumed to be representative of A04C. Similarly the radiometric observations at A04N1 and A04S1 were assumed to be representative of A04N and A04S. The agreement between ground observations and the SMRT base case is better for the pits where the radiometric observations were made i.e. A04C1, A04N1

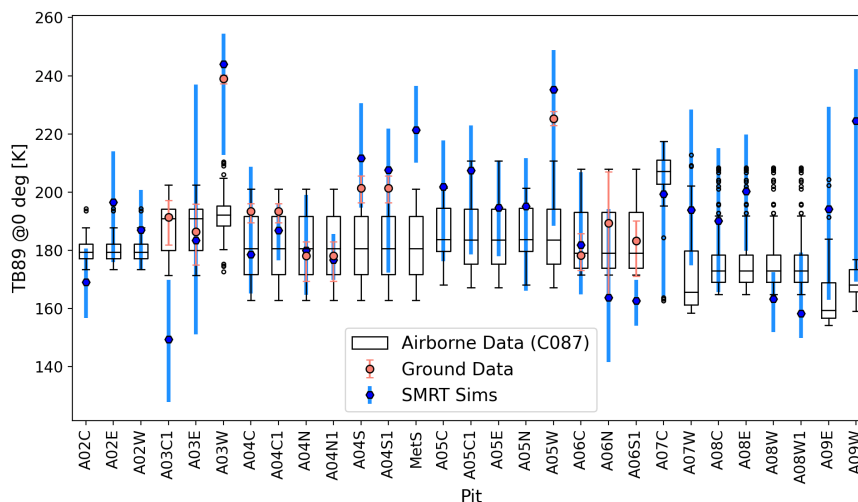


**Figure 7.** Comparison between SMRT simulations of microwave brightness temperature at 89 GHz, V-polarization, near-nadir incidence angle, ground-based measurements and flight C087 airborne observations from the MACSSIMIZE field campaign. SMRT and ground-based TB have been corrected to the height of the aircraft.

and A04S1. These adjacent pits in A04 give insight into the simulated microwave behaviour relative to the input data. At the central site simulated TB is lower at A04C than A04C1, which is consistent with the deeper snowpack and larger WS grains in A04C. The northern site is really interesting. TB at A04N is higher than at A04N1 despite smaller SSA (almost half that of  
 295 A04N1 in both WS and DH layers). This is in contrast to the expectation that smaller SSA means larger grains, more scattering and lower TB.

The Met Station pit was the only pit dug later than flights C087 and C090 and after a strong wind event (discussed later in this section) that redistributed snow, so simulations may not be representative of the airborne observations taken beforehand. However, analysis of post-wind event flight data shows similar results to the C087 and C090 flights, suggesting this may not  
 300 be the cause of the discrepancy. SSA observed at the Met Station were generally high, as shown in Table 2, but similar to pit A04N1. With Table 2 *missing data* SSA values applied to all layers, the base TB reduced from 221.3K to 213.0K. Conversely, pit A06S1 TB simulations are too low compared with both airborne and ground-based TB observations, which indicates too much scattering. Table 2 shows very low SSA for the WS layer (large grains), and values that would be more representative of depth hoar. If default *missing data* values were used for the SSA in all layers, TB increases from 162.6 K to 172.1 K, which  
 305 would be closer to the observations.

Figure 8 compares SMRT simulations with observations at frequencies between 89 and 243 GHz for the two flights (C087 and C090) over all snow pits, grouped by topographic type. TB range and sensitivity of observed TB to topography decreases with increasing frequency, indicating less dependence on surface properties. Observed TB variability generally decreases from flight C087 to C090 as shown by changes in interquartile range in Figure 8. Between flights there is little change in median TB

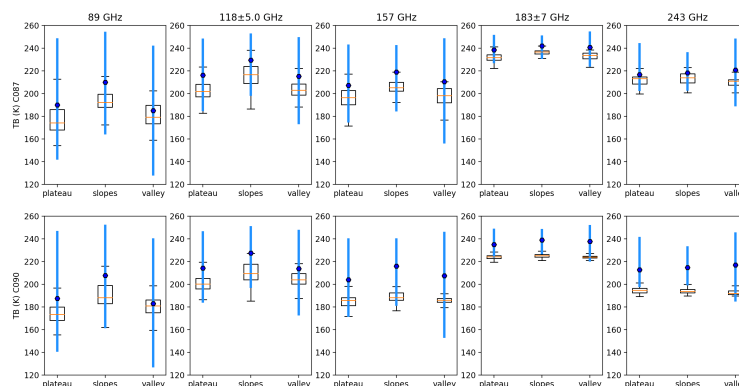


**Figure 8.** Box plot comparison between SMRT simulation (including atmosphere, corrected to aircraft height) and airborne observations at 89, 118, 157, 183 and 243 GHz grouped by topographic type. Results for the C087 flight are shown on the top and results for the C090 flight are shown on the bottom

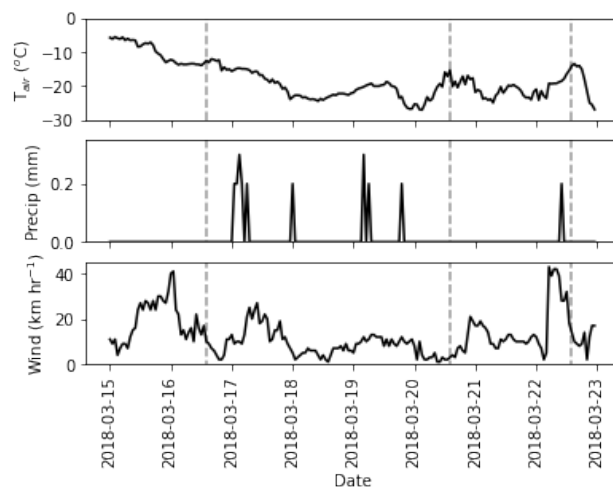


**Figure 9.** Hourly Meteorological data from Trail Valley station for duration of MACSSIMIZE campaign. Top: air temperature in degrees Celsius, Middle: Precipitation in mm, Bottom: Wind Speed in km hr<sup>-1</sup>. Dashed lines indicate flight timings: C087 on 16<sup>th</sup> March, C090 on 20<sup>th</sup> March and C092 on 22<sup>nd</sup> March 2018.

310 for 89 and 118 GHz, but a decrease at 157 GHz and above. SMRT simulations differ little between flights (only the atmospheric contribution changes in the simulations), leading to less overlap between simulations and observations at 183 and 243 GHz for flight C090.

Surface snowpack structure at the time of snowpit measurement may differ from the surface structure at the time of the flights. Figure 9 shows precipitation events and changes in air temperature and wind speed throughout the field campaign.





**Table 4.** Effect of thin surface snow layer on simulated median brightness temperatures for different topographical land surface types (K). Brightness temperature difference is calculated for snowpits with A03C1 surface snow minus snowpits as measured

Channel (GHz)	Slopes	Valley	Plateau
89	-0.8	0.6	0.4
118±5	-2.2	-0.1	-0.4
157	-9.5	-7.0	-6.2
183±7	-3.5	-2.8	-2.1
243	-13.3	-14.4	-12.4

315 Timings of three flights are also shown by the dashed vertical lines. After flight C087 on 16<sup>th</sup> March there were a number of snowfall events. Snow pit data from A03C1 on the 17<sup>th</sup> March (Table 2) indicates the surface snow had unusually low density of 40 kg m<sup>-3</sup>. Most snowpits after 17<sup>th</sup> March had surface snow densities of less than 100 kg m<sup>-3</sup>. Air temperature decreased after flight C087, with a cold spell between flight C087 and C090. Wind speed was relatively calm between flight C087 and C090 but there was a period of high wind speeds (maximum 43 km hr<sup>-1</sup>) between flight C090 on the 20<sup>th</sup> March and flight  
320 C092 on the 22<sup>nd</sup> March, which led to observed redistribution of surface snow after the blizzard, mostly removing snow above the ice lens in flat areas.

To examine the potential impact of surface change on TB and investigate whether this can account for the differences in observed TB between flights in Figure 8, a thin fresh surface snow layer was added to all snowpits. The additional surface snow layer was assumed to have similar properties to the surface layer of pit A03C1 i.e. thickness of 5 cm, density of 40 kg  
325 m<sup>-3</sup>, temperature of 260 K and exponential correlation length of 0.1 mm. The difference in TB is shown for each frequency in Table 4, and is shown in the Supplementary Material Figure A2. Additional surface snow decreases the brightness temperatures at all frequencies. The absolute difference is small (<2.2 K) at 89 and 118 GHz, moderate at 183 GHz (2.1-3.5 K) and larger at 157 and 243 GHz (6.2-14.4 K). Given that the penetration depth decreases with frequency it could be expected that the effect of the surface layer should increase with frequency, but this is not the case for 183 GHz, where the effect is smaller than at  
330 157 GHz. This suggests that emission from the atmosphere itself may dominate over the impact of the additional surface snow layer at 183 GHz.

The importance of including the atmosphere at different frequencies is demonstrated in Figure 10. Overall, inclusion of the atmosphere reduces the RMSE of the base simulation medians by frequency and flight from 23 K to 14 K. The impact of the atmosphere is largest at 183 GHz and smallest at 89 GHz. Inclusion of the atmosphere narrows the range of simulated  
335 TB. Atmospheric emission increases simulated TB, as shown by the shift in median (from blue to red dashed lines in Figure 10) despite atmospheric attenuation of emitted radiation from the snow surface. For all frequencies, median TB including the atmosphere is closer to the observations than simulations without the atmosphere. However, Kolmogorov-Smirnov 2-sample tests of distribution equivalence show that both simulated distributions (with and without atmosphere) differ from the distribution of airborne observations at a 5% level.

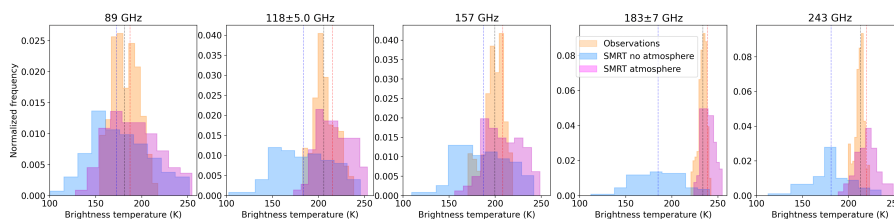


**Figure 10.** Histogram of brightness temperatures for all frequencies showing the impact of neglecting atmospheric contribution in SMRT simulations. Observations are for flight C087 only, aggregated over AOI and topographical surface type. Dashed lines show distribution medians: black for observations, blue for SMRT with no atmosphere and red for SMRT simulations incorporating atmospheric effects

#### 340 4 Discussion

The aim of this study was to evaluate whether SMRT could be used to explain observed microwave behaviour at frequencies needed to improve numerical weather prediction in the Arctic. With anisotropic atmospheric emission and attenuation modelled with ARTS, SMRT captures the distinction between snow overlying different topography. The frequency dependence is also simulated well. The good agreement here supports the applicability of IBA electromagnetic theory at higher frequencies. With the limit of wavenumber  $k_0 \sim 1.5 \times \text{radius}$  (Picard et al., 2022), the IBA upper frequency limit for the largest scattering depth hoar layer in Table 2 i.e.  $8.6 \text{ m}^2 \text{ kg}^{-1}$  is around 188 GHz. Inclusion of the atmosphere reduces simulated RMSE to a value that could be expected from comparisons with ground-based observations at frequencies more sensitive to snow. An RMSE of 14 K for the base simulations here is within the range of 13-26 K reported in the literature in the frequency range 19-89 GHz (Roy et al., 2016; Royer et al., 2017; Vargel et al., 2020) given similar in situ microstructure data.

350 Underlying topography is relevant at 89 GHz but becomes less relevant at higher frequencies. As the frequency increases, the penetration depth reduces and the sensor may only see the upper portion of snowpack. This is the dominant effect. However, the depth of snow (influenced by topography) may be relevant as it directly affects microwave scattering and controls the temperature gradient and therefore rate of grain growth. Local topography and slopes affect the snowpack energy balance and may also reduce or enhance densification depending on their orientation relative to the wind direction. These structural changes in the snowpack that are influenced by topography may result in a topographical signal in the TB despite the signal not penetrating to the base of the snowpack.

Variability in ground observations of microstructure lead to a large variation in simulated TB and good overlap with airborne observations for the majority of snow pits. This demonstrates the value of making multiple measurements within the snowpack as the simulations cover a range of plausible TBs at a point given the best available snowpack structure information. Kolmogorov-Smirnov tests show that the simulations and airborne observations have different distributions even with the atmosphere taken into account. This may be expected as airborne observations capture more of the terrain than individual pits, which were chosen to maximise variability rather than provide random statistical sampling of the region (which would not be feasible given the number of pits required to do so). There is an issue of scale, as simulations use point measurements, whereas the airborne footprint covers an area of up to  $\sim 100 \text{ m}$  in diameter. Whilst snowpit simulations should lie within the range of



365 airborne simulations and for the most part do, it is possible that the differences in ground footprint location mean that snow  
conditions in the snowpits were not sampled along the aircraft transects. In some cases there are clear differences in location  
(Figure 6) and pits A03W and A05W were located in drifts not captured in the airborne transect. The spatial extent of the drift  
is also smaller than the airborne footprint, so even if the flight transect had completed a direct overpass, the drift contribution  
to airborne observations may be limited. Further improvements could be gained with a better understanding of how to relate pit  
370 measurements to larger scale microstructure variability. This may be possible with rapid measurement instruments such as the  
snow micropenetrator in conjunction with local pit calibration as demonstrated by King et al. (2020); Dutch et al. (2022).

It is crucial to know the relative thickness of layers as these can override microstructural differences by changing the penetra-  
tion into lower, larger grain size layers. This is demonstrated by the paired pits in A04N and A04N1, where A04N TB was  
higher than at A04N1 despite smaller SSA (i.e. larger grains, more scattering) in A04N snowpit layers. The difference here  
375 is driven by the thinner WS layer in A04N1. More of the signal is proportionally affected by the DH grains than for A04N,  
leading to lower TB. The importance of the relative thickness of the depth hoar layer has already been highlighted in other  
studies (King et al., 2018; Rutter et al., 2019; Meloche et al., 2022) and is consistent with the higher sensitivity of surface layer  
changes at 94 GHz compared to lower frequencies found by Wiesmann et al. (2000).

Identification of small precipitation events with deposition of low density, small grain size surface snow will be important  
380 for use of these data in NWP. Although atmospheric conditions differ between the two flight days, the differences are too small  
to explain the low TB observed in flight C090. A change in microstructure rather than a change in atmospheric conditions may  
explain the difference in observed TB. Meteorological and in situ data presented here suggest deposition of low-density snow  
between the first two flights that was then removed, redistributed or was heavily compacted by wind between the second and  
third flights leading to similar observed TB for the first and third flights but lower TB for the middle flight. Smooth surface ice  
385 lenses facilitated wind redistribution and removal of the surface snow. Addition of a thin, low-density fresh surface snow in the  
simulations supports the hypothesis that the difference in observed TB is driven by snow microstructural differences between  
flights. In the simulations the mass of snow added is small and the exponential correlation length is also small, which means  
that the scattering within that layer is small. The difference in brightness temperature is likely due to the high (density-driven)  
dielectric contrast between layers caused by the unusually low-density fresh snow. The effect is largest at 243 GHz, where  
390 penetration depth is smallest. The difference at 183 GHz could be expected to exceed that at 157 GHz because of the shallower  
penetration depth at the higher frequency. It does not because the effect of the atmosphere is larger at 183 GHz.

The demonstrated ability of SMRT to represent TB variability over different snow-covered topography in TVC indicates the  
potential value of using SMRT to improve atmospheric retrievals given snowpack information. In general there is good overlap  
with observations, with some differences between simulated TB and airborne measurements that can be explained by local  
395 variability in microstructure, changing meteorological conditions, differences in measurement location and/or footprint size. In  
current numerical weather prediction models, microwave emissivity is assumed to be constant over snow-covered surfaces or  
derived from a monthly climatology, with errors too large to be able to use satellite observations in the Arctic. Instead, SMRT  
could be used to parameterise the surface radiometric behaviour. This would require good microstructure, layer thicknesses and  
identification of surface snow from the NWP land surface model. Optimising assimilation of satellite observations has been



400 identified as the most effective way to improve forecast skill in the Arctic (Laroche and Poan, 2022). NWP systems already use radiative transfer models but require higher accuracy models for snow (e.g. vertical polarisation bias at 89 GHz is currently  $\sim -35$  K: Hirahara et al., 2020, Figure 13). This should be possible with SMRT. Future work will focus on how we can use SMRT to quantify observation uncertainty from satellite measurements at microwave frequencies over snow-covered regions and consequently how to use the atmospheric information within them to improve weather forecasts in the Arctic.

## 405 5 Conclusions

In this study SMRT was evaluated at frequencies between 89 and 243 GHz in an Arctic tundra snow environment with the atmospheric contribution estimated with ARTS. It was found that there was good agreement between simulations and airborne observations despite differences in footprint location and size. At 243 GHz, the electromagnetic model used is potentially outside the range of applicability, but the good agreement may be partly because the larger grain sizes that start to approach  
410 the wavelength of radiation are located deeper in the pack and therefore contribute less to the signal as the penetration depth decreases. Inclusion of the atmospheric emission and scattering, such as with ARTS, is essential for accurate simulation and interpretation of ground-based, airborne and satellite observations of microwave emission at surface-sensitive atmosphere channels.

Here, a clear topography-related signal was evident at the lower frequencies, but the distinction between sloped, valley and  
415 plateau areas diminished as frequency increased. This is because the penetration depth of radiation decreases with frequency and at higher frequencies, less of the signal comes from the lower portion of the snowpack. Differences between adjacent snowpacks demonstrated that in addition to microstructure, accurate knowledge of layer thickness is also critical to determine whether the deeper snow layers are seen by the sensors. The ability of snowpack models to simulate these parameters is an important area of research, particularly for land surface models used in Numerical Weather Prediction systems.

420 Spatial variation in brightness temperatures observed with airborne instruments is reflected by the simulations, which indicates potential for use of SMRT to interpret satellite observations needed for Numerical Weather Prediction. Meteorological events i.e. the addition of fresh, low density precipitation and a later wind event that removed it over the space of a few days caused differences in observed brightness temperatures. The effects of this event were largest at 157 GHz and 243 GHz as the signal is more weighted to the surface of the snow, but somewhat dampened by the atmospheric contribution at 183 GHz.  
425 This study has shown how snow microstructural and stratigraphic information can have different influences depending on the frequency of observations used. A strategy to account for both spatial and temporal variability in snow microstructure is much needed for future implementation in Numerical Weather Prediction systems, and allow use of Arctic microwave satellite observations in weather forecasts.



430 *Code and data availability.* Code and data to repeat these simulations are available at [git@github.com:mjsandells/AESOP\\_paper.git](https://github.com:mjsandells/AESOP_paper.git). Meteorological data for Figure 9 can be downloaded from [https://climate.weather.gc.ca/historical\\_data/search\\_historic\\_data\\_e.html](https://climate.weather.gc.ca/historical_data/search_historic_data_e.html) for station Trail Valley (WMO ID 71683), March 2018.

435 *Author contributions.* MS, NR, SF designed the study and wrote the AESOP proposal; MS and KW performed the SMRT simulations and data analysis; KW and SF coupled ARTS to SMRT; CH, NR, PT and RE planned and coordinated the combined airborne and ground-based field campaign; NR, RE, AR<sup>2</sup> and PT made ground-based field observations; SF and CH made airborne observations; GP assisted with analysis and interpretation. All contributed to writing this paper.

*Competing interests.* The authors declare that there are no competing interests.

440 *Acknowledgements.* This project was funded by NERC (Grant No. NE/S009280/1: Arctic Emissivity of Snow for Operational Prediction of Weather: AESOP). Data collection was made possible thanks to NERC Arctic Office UK and the Canada Arctic Partnership Bursaries Programme (to NR and RE), Wilfrid Laurier University (Phil Marsh and Branden Walker) and Environment and Climate Change Canada. The radiometric surface-based measurements have been supported by the Natural Sciences and Engineering Research Council of Canada (NSERC) and by Polar Knowledge Canada. We thank Arvids Silis, Branden Walker and Evan Wilcox for indispensable field logistics and measurement support and Chris Derksen for help in planning the fieldwork. The MACSSIMIZE campaign was part of the Year of Polar Prediction effort, coordinated by the WMO Polar Prediction Project.



## Appendix A: Supplementary Figures

**Figure A1.** Simulated (blue) vs observed mean and range (grey) downwelling brightness temperatures at the full range of zenith view angles, averaged across the AOIs at 89,  $118\pm 5.0$ , 157,  $183\pm 7$ , and 243 GHz for flight C087 (a) and C090 (b). Mean Absolute Errors are given for each channel in each flight.

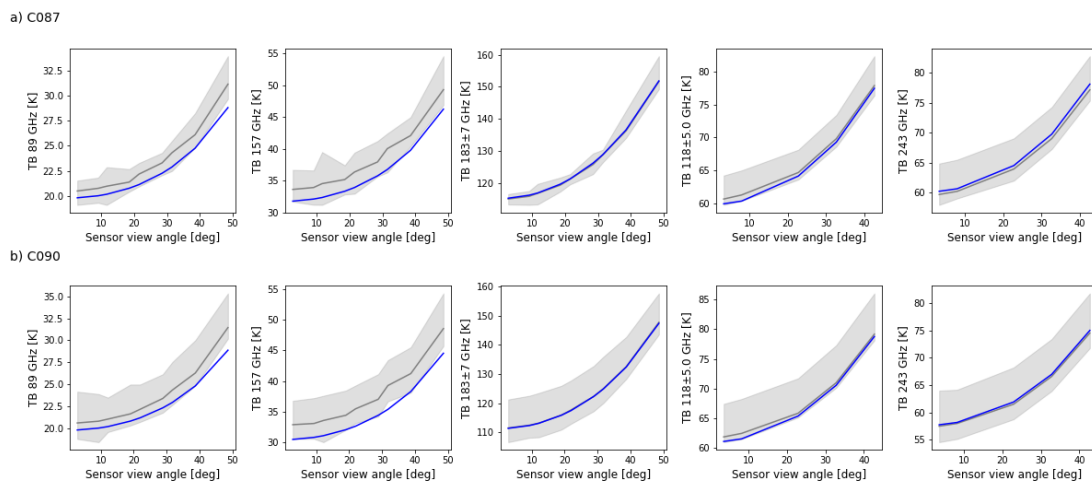
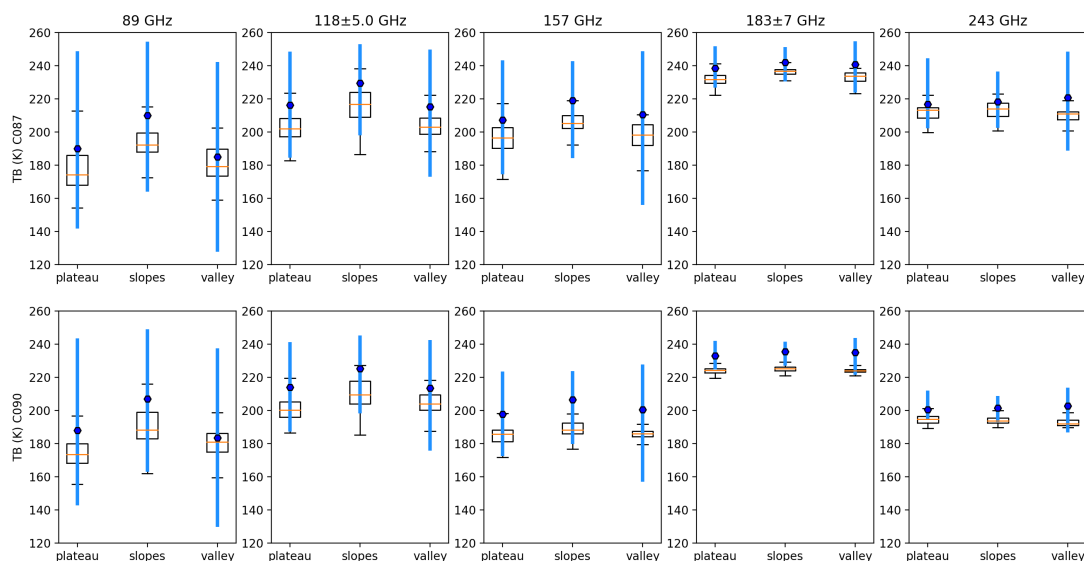




**Figure A2.** Box plot comparison between SMRT simulation (including atmosphere, corrected to aircraft height) and airborne observations at 89, 118, 157, 183 and 243 GHz grouped by topographic type. Results for the C087 flight are shown on the top and results for the C090 flight are shown on the bottom. A thin surface snow layer has been added for flight C090 simulations.





## 445 References

- Baordo, F. and Geer, A. J.: Assimilation of SSMIS humidity-sounding channels in all-sky conditions over land using a dynamic emissivity retrieval, *Quarterly Journal of the Royal Meteorological Society*, 142, 2854–2866, <https://doi.org/https://doi.org/10.1002/qj.2873>, <https://rmets.onlinelibrary.wiley.com/doi/abs/10.1002/qj.2873>, \_eprint: <https://rmets.onlinelibrary.wiley.com/doi/pdf/10.1002/qj.2873>, 2016.
- Bauer, P., Magnusson, L., Thépaut, J.-N., and Hamill, T. M.: Aspects of ECMWF model performance in polar areas, *Quarterly Journal of the Royal Meteorological Society*, 142, 583–596, <https://doi.org/https://doi.org/10.1002/qj.2449>, <https://rmets.onlinelibrary.wiley.com/doi/abs/10.1002/qj.2449>, \_eprint: <https://rmets.onlinelibrary.wiley.com/doi/pdf/10.1002/qj.2449>, 2016.
- 450 Bormann, N., Lupu, C., Geer, A., Lawrence, H., Weston, P., and English, S.: Assessment of the forecast impact of surface-sensitive microwave radiances over land and sea-ice, Tech. Rep. 804, European Centre for Medium Range Weather Forecasts, 2017.
- Buehler, S. A., Mendrok, J., Eriksson, P., Perrin, A., Larsson, R., and Lemke, O.: ARTS, the Atmospheric Radiative Transfer Simulator – version 2.2, the planetary toolbox edition, *Geosci. Model Dev.*, 11, 1537–1556, <https://doi.org/10.5194/gmd-11-1537-2018>, <https://www.geosci-model-dev.net/11/1537/2018/>, 2018.
- 455 Cohen, J., Screen, J. A., Furtado, J. C., Barlow, M., Whittleston, D., Coumou, D., Francis, J., Dethloff, K., Entekhabi, D., Overland, J., and Jones, J.: Recent Arctic amplification and extreme mid-latitude weather, *Nature Geoscience*, 7, 627–637, <https://doi.org/10.1038/ngeo2234>, <https://www.nature.com/articles/ngeo2234>, number: 9 Publisher: Nature Publishing Group, 2014.
- 460 Day, J. J., Sandu, I., Magnusson, L., Rodwell, M. J., Lawrence, H., Bormann, N., and Jung, T.: Increased Arctic influence on the midlatitude flow during Scandinavian Blocking episodes, *Quarterly Journal of the Royal Meteorological Society*, 145, 3846–3862, <https://doi.org/10.1002/qj.3673>, <https://onlinelibrary.wiley.com/doi/abs/10.1002/qj.3673>, \_eprint: <https://onlinelibrary.wiley.com/doi/pdf/10.1002/qj.3673>, 2019.
- Ding, K.-H., Xu, X., and Tsang, L.: Electromagnetic Scattering by Bicontinuous Random Microstructures With Discrete Permittivities, *IEEE Transactions on Geoscience and Remote Sensing*, 48, 3139–3151, <https://doi.org/10.1109/TGRS.2010.2043953>, 2010.
- 465 Dutch, V. R., Rutter, N., Wake, L., Sandells, M., Derksen, C., Walker, B., Hould Gosselin, G., Sonnentag, O., Essery, R., Kelly, R., Marsh, P., King, J., and Boike, J.: Impact of measured and simulated tundra snowpack properties on heat transfer, *The Cryosphere*, 16, 4201–4222, <https://doi.org/10.5194/tc-16-4201-2022>, <https://tc.copernicus.org/articles/16/4201/2022/>, publisher: Copernicus GmbH, 2022.
- Eriksson, P., Buehler, S. A., Davis, C. P., Emde, C., and Lemke, O.: ARTS, the Atmospheric Radiative Transfer Simulator, Version 2, *Journal of Quantitative Spectroscopy and Radiative Transfer*, 112, 1551–1558, <https://doi.org/https://doi.org/10.1016/j.jqsrt.2011.03.001>, <https://www.sciencedirect.com/science/article/pii/S0022407311001105>, 2011.
- 470 Fierz, C., Armstrong, R. L., Durand, Y., Etchevers, P., Greene, E., McClung, D. M., Nishimura, K., Satyawali, P. K., and Sokratov, S. A.: The international classification for seasonal snow on the ground, UNESCO/IHP, 2009.
- Fox, S., Lee, C., Moyna, B., Philipp, M., Rule, I., Rogers, S., King, R., Oldfield, M., Rea, S., Henry, M., Wang, H., and Harlow, R. C.: ISMAR: an airborne submillimetre radiometer, *Atmos. Meas. Tech.*, 10, 477–490, <https://doi.org/https://doi.org/10.5194/amt-10-477-2017>, <https://www.atmos-meas-tech.net/10/477/2017/>, 2017.
- Francis, J. A. and Vavrus, S. J.: Evidence linking Arctic amplification to extreme weather in mid-latitudes, *Geophysical Research Letters*, 39, <https://doi.org/https://doi.org/10.1029/2012GL051000>, <https://agupubs.onlinelibrary.wiley.com/doi/abs/10.1029/2012GL051000>, \_eprint: <https://agupubs.onlinelibrary.wiley.com/doi/pdf/10.1029/2012GL051000>, 2012.
- 480 Gallet, J.-C., Domine, F., Zender, C., and Picard, G.: Measurement of the specific surface area of snow using infrared reflectance in an integrating sphere at 1310 and 1550 nm, *The Cryosphere*, 3, 167–182, 2009.





- Geer, A. J., Fabrizio, B., Bormann, N., and English, S.: All-sky assimilation of microwave humidity sounders, Tech. Rep. 741, European Centre for Medium-Range Weather Forecasts, 2014.
- 485 Guedj, S., Karbou, F., Rabier, F., and Bouchard, A.: Toward a Better Modeling of Surface Emissivity to Improve AMSU Data Assimilation Over Antarctica, *IEEE Transactions on Geoscience and Remote Sensing*, 48, 1976–1985, <https://doi.org/10.1109/TGRS.2009.2036254>, 2010.
- Han, Y. and Westwater, E. R.: Analysis and improvement of tipping calibration for ground-based microwave radiometers, *IEEE Transactions on Geoscience and Remote Sensing*, 38, 1260–1276, <https://doi.org/https://doi.org/10.1109/36.843018>, <https://ieeexplore.ieee.org/document/843018>, 2000.
- 490 Harlow, R. and Essery, R.: Tundra Snow Emissivities at MHS Frequencies: MEMLS Validation Using Airborne Microwave Data Measured During CLPX-II, *IEEE Transactions on Geoscience and Remote Sensing*, 50, 4262–4278, <https://doi.org/10.1109/TGRS.2012.2193132>, 2012.
- Hirahara, Y., Rosnay, P. d., and Arduini, G.: Evaluation of a Microwave Emissivity Module for Snow Covered Area with CMEM in the ECMWF Integrated Forecasting System, *Remote Sensing*, 12, 2946, <https://doi.org/10.3390/rs12182946>, <https://www.mdpi.com/2072-4292/12/18/2946>, number: 18 Publisher: Multidisciplinary Digital Publishing Institute, 2020.
- 495 Karbou, F., Rabier, F., and Prigent, C.: The Assimilation of Observations from the Advanced Microwave Sounding Unit over Sea Ice in the French Global Numerical Weather Prediction System, *Monthly Weather Review*, 142, 125–140, <https://doi.org/10.1175/MWR-D-13-00025.1>, <https://journals.ametsoc.org/view/journals/mwre/142/1/mwr-d-13-00025.1.xml>, publisher: American Meteorological Society Section: Monthly Weather Review, 2014.
- 500 King, J., Derksen, C., Toose, P., Langlois, A., Larsen, C., Lemmetyinen, J., Marsh, P., Montpetit, B., Roy, A., Rutter, N., and Sturm, M.: The influence of snow microstructure on dual-frequency radar measurements in a tundra environment, *Remote Sensing of Environment*, 215, 242–254, <https://doi.org/10.1016/j.rse.2018.05.028>, <https://www.sciencedirect.com/science/article/pii/S003442571830258X>, 2018.
- King, J., Howell, S., Brady, M., Toose, P., Derksen, C., Haas, C., and Beckers, J.: Local-scale variability of snow density on Arctic sea ice, *The Cryosphere*, 14, 4323–4339, <https://doi.org/10.5194/tc-14-4323-2020>, <https://tc.copernicus.org/articles/14/4323/2020/>, publisher: Copernicus GmbH, 2020.
- 505 Langlois, A.: Applications of the PR series Radiometers for cryospheric and Soil Moisture Research, Radiometrics Corporation, Colorado, p. 40, 2015.
- Laroche, S. and Poan, E. D.: Impact of the Arctic observing systems on the ECCO global weather forecasts, *Quarterly Journal of the Royal Meteorological Society*, 148, 252–271, <https://doi.org/10.1002/qj.4203>, <https://onlinelibrary.wiley.com/doi/abs/10.1002/qj.4203>, [\\_eprint: https://onlinelibrary.wiley.com/doi/pdf/10.1002/qj.4203](https://onlinelibrary.wiley.com/doi/pdf/10.1002/qj.4203), 2022.
- 510 Larue, F., Picard, G., Aublanc, J., Arnaud, L., Robledano-Perez, A., LE Meur, E., Favier, V., Jourdain, B., Savarino, J., and Thibaut, P.: Radar altimeter waveform simulations in Antarctica with the Snow Microwave Radiative Transfer Model (SMRT), *Remote Sensing of Environment*, 263, 112 534, <https://doi.org/10.1016/j.rse.2021.112534>, <https://www.sciencedirect.com/science/article/pii/S0034425721002546>, 2021.
- 515 Lawrence, H., Bormann, N., Sandu, I., Day, J., Farnan, J., and Bauer, P.: Use and impact of Arctic observations in the ECMWF Numerical Weather Prediction system, *Quarterly Journal of the Royal Meteorological Society*, 145, 3432–3454, <https://doi.org/https://doi.org/10.1002/qj.3628>, <https://rmets.onlinelibrary.wiley.com/doi/abs/10.1002/qj.3628>, [\\_eprint: https://rmets.onlinelibrary.wiley.com/doi/pdf/10.1002/qj.3628](https://rmets.onlinelibrary.wiley.com/doi/pdf/10.1002/qj.3628), 2019.



- Leinss, S., Löwe, H., Proksch, M., and Kontu, A.: Modeling the evolution of the structural anisotropy of snow, *The Cryosphere*, 14, 51–75,  
520 <https://doi.org/10.5194/tc-14-51-2020>, <https://tc.copernicus.org/articles/14/51/2020/>, 2020.
- Lemmetyinen, J., Pulliainen, J., Rees, A., Kontu, A., Qiu, Y., and Derksen, C.: Multiple-Layer Adaptation of HUT Snow Emission Model: Comparison With Experimental Data, *IEEE Transactions on Geoscience and Remote Sensing*, 48, 2781–2794,  
<https://doi.org/10.1109/TGRS.2010.2041357>, 2010.
- Löwe, H. and Picard, G.: Microwave scattering coefficient of snow in MEMLS and DMRT-ML revisited: The relevance of sticky hard  
525 spheres and tomography-based estimates of stickiness, *The Cryosphere*, 9, 2101–2117, 2015.
- McGrath, A. and Hewison, T.: Measuring the accuracy of MARSS—an airborne microwave radiometer, *J. Atmos. Ocean.*, 18, 2003–  
2012, [https://doi.org/https://doi.org/10.1175/1520-0426\(2001\)018<2003:MTAOMA>2.0.CO;2](https://doi.org/https://doi.org/10.1175/1520-0426(2001)018<2003:MTAOMA>2.0.CO;2), <https://journals.ametsoc.org/doi/full/10.1175/1520-0426%282001%29018%3C2003%3AMTAOMA%3E2.0.CO%3B2>, 2001.
- Meloche, J., Langlois, A., Rutter, N., Royer, A., King, J., Walker, B., Marsh, P., and Wilcox, E. J.: Characterizing tundra snow sub-pixel variability to improve brightness temperature estimation in satellite SWE retrievals, *The Cryosphere*, 16, 87–101, <https://doi.org/10.5194/tc-16-87-2022>, <https://tc.copernicus.org/articles/16/87/2022/>, publisher: Copernicus GmbH, 2022.
- 530 Montpetit, B., Royer, A., Langlois, A., Cliche, P., Roy, A., Champollion, N., Picard, G., Domine, F., and Obbard, R.: New shortwave infrared albedo measurements for snow specific surface area retrieval, *Journal of Glaciology*, 58, 941–952, <https://doi.org/10.3189/2012JoG11J248>, 2012.
- 535 Mätzler, C.: Relation between grain-size and correlation length of snow, *Journal of Glaciology*, 48, 461–466, <https://doi.org/10.3189/172756502781831287>, 2002.
- Overland, J., Francis, J. A., Hall, R., Hanna, E., Kim, S.-J., and Vihma, T.: The Melting Arctic and Midlatitude Weather Patterns: Are They Connected?, *Journal of Climate*, 28, 7917–7932, <https://doi.org/10.1175/JCLI-D-14-00822.1>, <https://journals.ametsoc.org/view/journals/clim/28/20/jcli-d-14-00822.1.xml>, publisher: American Meteorological Society Section: Journal of Climate, 2015.
- 540 Overland, J. E., Ballinger, T. J., Cohen, J., Francis, J. A., Hanna, E., Jaiser, R., Kim, B.-M., Kim, S.-J., Ukita, J., Vihma, T., Wang, M., and Zhang, X.: How do intermittency and simultaneous processes obfuscate the Arctic influence on midlatitude winter extreme weather events?, *Environ. Res. Lett.*, 16, 043 002, <https://doi.org/10.1088/1748-9326/abdb5d>, <https://doi.org/10.1088/1748-9326/abdb5d>, publisher: IOP Publishing, 2021.
- Pan, J., Durand, M., Sandells, M., Lemmetyinen, J., Kim, E., Pulliainen, J., Kontu, A., and Derksen, C.: Differences Between the HUT Snow  
545 Emission Model and MEMLS and Their Effects on Brightness Temperature Simulation, *IEEE Transactions on Geoscience and Remote Sensing*, PP, 1–19, <https://doi.org/10.1109/TGRS.2015.2493505>, 2015.
- Picard, G., Brucker, L., Roy, A., Dupont, F., Fily, M., Royer, A., and Harlow, C.: Simulation of the microwave emission of multi-layered snowpacks using the Dense Media Radiative transfer theory: the DMRT-ML model, *Geosci. Model Dev.*, 6, 1061–1078,  
<https://doi.org/10.5194/gmd-6-1061-2013>, <http://www.geosci-model-dev.net/6/1061/2013/>, 2013.
- 550 Picard, G., Sandells, M., and Löwe, H.: SMRT: an active–passive microwave radiative transfer model for snow with multiple microstructure and scattering formulations (v1.0), *Geoscientific Model Development*, 11, 2763–2788, <https://doi.org/10.5194/gmd-11-2763-2018>, <https://www.geosci-model-dev.net/11/2763/2018/>, 2018.
- Picard, G., Löwe, H., and Mätzler, C.: Brief communication: A continuous formulation of microwave scattering from fresh snow to bubbly  
555 ice from first principles, *The Cryosphere*, 16, 3861–3866, <https://doi.org/10.5194/tc-16-3861-2022>, <https://tc.copernicus.org/articles/16/3861/2022/>, publisher: Copernicus GmbH, 2022.



- Pithan, F., Svensson, G., Caballero, R., Chechin, D., Cronin, T. W., Ekman, A. M. L., Neggers, R., Shupe, M. D., Solomon, A., Tjernström, M., and Wendisch, M.: Role of air-mass transformations in exchange between the Arctic and mid-latitudes, *Nature Geoscience*, 11, 805–812, <https://doi.org/10.1038/s41561-018-0234-1>, <https://www.nature.com/articles/s41561-018-0234-1>, number: 11 Publisher: Nature Publishing Group, 2018.
- 560 Randriamampianina, R., Bormann, N., Körtzow, M. A. , Lawrence, H., Sandu, I., and Wang, Z. Q.: Relative impact of observations on a regional Arctic numerical weather prediction system, *Quarterly Journal of the Royal Meteorological Society*, 147, 2212–2232, <https://doi.org/10.1002/qj.4018>, <https://onlinelibrary.wiley.com/doi/abs/10.1002/qj.4018>, 2021.
- Roy, A., Royer, A., St-Jean-Rondeau, O., Montpetit, B., Picard, G., Mavrovic, A., Marchand, N., and Langlois, A.: Microwave snow emission modeling uncertainties in boreal and subarctic environments, *The Cryosphere*, 10, 623–638, <https://doi.org/10.5194/tc-10-623-2016>, <https://tc.copernicus.org/articles/10/623/2016/>, publisher: Copernicus GmbH, 2016.
- 565 Royer, A., Roy, A., Montpetit, B., Saint-Jean-Rondeau, O., Picard, G., Brucker, L., and Langlois, A.: Comparison of commonly-used microwave radiative transfer models for snow remote sensing, *Remote Sensing of Environment*, 190, 247 – 259, <https://doi.org/https://doi.org/10.1016/j.rse.2016.12.020>, <http://www.sciencedirect.com/science/article/pii/S0034425716304990>, 2017.
- Rutter, N., Sandells, M. J., Derksen, C., King, J., Toose, P., Wake, L., Watts, T., Essery, R., Roy, A., Royer, A., Marsh, P., Larsen, C., and Sturm, M.: Effect of snow microstructure variability on Ku-band radar snow water equivalent retrievals, *The Cryosphere*, 13, 3045–3059, <https://doi.org/https://doi.org/10.5194/tc-13-3045-2019>, <https://www.the-cryosphere.net/13/3045/2019/>, publisher: Copernicus GmbH, 2019.
- 570 Sandells, M., Essery, R., Rutter, N., Wake, L., Leppänen, L., and Lemmetyinen, J.: Microstructure representation of snow in coupled snowpack and microwave emission models, *The Cryosphere*, 11, 229–246, <https://doi.org/10.5194/tc-11-229-2017>, <https://www.the-cryosphere.net/11/229/2017/>, 2017.
- Sandells, M., Löwe, H., Picard, G., Dumont, M., Essery, R., Floury, N., Kontu, A., Lemmetyinen, J., Maslanka, W., Morin, S., Wiesmann, A., and Mätzler, C.: X-Ray Tomography-Based Microstructure Representation in the Snow Microwave Radiative Transfer Model, *IEEE Transactions on Geoscience and Remote Sensing*, pp. 1–15, <https://doi.org/10.1109/TGRS.2021.3086412>, conference Name: IEEE Transactions on Geoscience and Remote Sensing, 2021.
- 580 Tretyakov, M. Y., Koshelev, M. A., Dorovskikh, V. V., Makarov, D. S., and Rosenkranz, P. W.: 60-GHz oxygen band: precise broadening and central frequencies of fine-structure lines, absolute absorption profile at atmospheric pressure, and revision of mixing coefficients, *Journal of Molecular Spectroscopy*, 231, 1–14, <https://doi.org/10.1016/j.jms.2004.11.011>, <https://www.sciencedirect.com/science/article/pii/S0022285204003650>, 2005.
- Tsang, L., Chen, C.-T., Chang, A. T. C., Guo, J., and Ding, K.-H.: Dense media radiative transfer theory based on quasicrystalline approximation with applications to passive microwave remote sensing of snow, *Radio Science*, 35, 731–749, <https://doi.org/10.1029/1999RS002270>, <http://onlinelibrary.wiley.com/doi/10.1029/1999RS002270/abstract>, 2000.
- 585 Vargel, C., Royer, A., St-Jean-Rondeau, O., Picard, G., Roy, A., Sasseville, V., and Langlois, A.: Arctic and subarctic snow microstructure analysis for microwave brightness temperature simulations, *Remote Sensing of Environment*, 242, 111 754, <https://doi.org/10.1016/j.rse.2020.111754>, <http://www.sciencedirect.com/science/article/pii/S0034425720301243>, 2020.
- 590 Walker, B., Wilcox, E. J., and Marsh, P.: Accuracy assessment of late winter snow depth mapping for tundra environments using Structure-from-Motion photogrammetry, *Arctic Science*, 7, 588–604, <https://doi.org/10.1139/as-2020-0006>, <https://cdnsiencepub.com/doi/10.1139/as-2020-0006>, publisher: NRC Research Press, 2021.



- Wang, D., Prigent, C., Kilic, L., Fox, S., Harlow, C., Jimenez, C., Aires, F., Grassotti, C., and Karbou, F.: Surface Emissivity at Microwaves to Millimeter Waves over Polar Regions: Parameterization and Evaluation with Aircraft Experiments, *J. Atmos. Oceanic Technol.*, 34, 1039–1059, <https://doi.org/10.1175/JTECH-D-16-0188.1>, <https://journals.ametsoc.org/jtech/article/34/5/1039/39853/Surface-Emissivity-at-Microwaves-to-Millimeter>, publisher: American Meteorological Society, 2017.
- Watts, T., Rutter, N., Toose, P., Derksen, C., Sandells, M., and Woodward, J.: Brief communication: Improved measurement of ice layer density in seasonal snowpacks, *The Cryosphere*, 10, 2069–2074, <https://doi.org/10.5194/tc-10-2069-2016>, <https://tc.copernicus.org/articles/10/2069/2016/>, publisher: Copernicus GmbH, 2016.
- Wiesmann, A. and Mätzler, C.: Microwave Emission Model of Layered Snowpacks, *Remote Sensing of Environment*, 70, 307–316, [https://doi.org/10.1016/S0034-4257\(99\)00046-2](https://doi.org/10.1016/S0034-4257(99)00046-2), <http://www.sciencedirect.com/science/article/pii/S0034425799000462>, 1999.
- Wiesmann, A., Fierz, C., and Mätzler, C.: Simulation of microwave emission from physically modeled snowpacks, *Annals of Glaciology*, 31, 397–405, <https://doi.org/10.3189/172756400781820453>, 2000.